KEYNOTE ADDRESS

# RELATIVE ELEVATION DETERMINATION FROM LANDSAT IMAGERY

R.M. Haralick, S. Wang

Dept. of Electrical Engineering and Computer Science

Virginia Polytechnic Institute and State University

ABSTRACT - In LANDSAT imagery, spectral and spatial information can be used to detect the drainage network as well as the relative elevation model in mountainous terrain. To do this, the mixed information of material reflectance and topographic modulation in the original LANDSAT imagery must be first separated. From the material reflectance information, big visible rivers can be detected. From the topographic modulation information, ridges and valleys can be detected and assigned relative elevations. Finally, a relative elevation model can be generated by interpolating values for non-ridge and non-valley pixels.

PROCEEDINGS OF THE NASA SYMPOSIUM ON
MATHEMATICA PATTERN RECOGNITION & IMAGE ANALYSIS
JUNE 1-3 JOHNSON SPACE CENTER, HOUSTON TX

## 1. Introduction

It is a common task for a photointerpreter to examine the spatial pattern on an aerial image and by appropriate interpretation be able to tell the elevation of one area relative to another and be able to infer the stream network and the drainage network even though some of the streams may be below the resolution of the sensor. There is a wealth of information in spatial patterns on aerial imagery but most computer data processing of remotely sensed imagery, being limited to pixel spectral characteristics, does not make use of it.

In this paper, we describe a procedure by which a relative elevation model can be infered from a LANDSAT scene of mountainous and hilly terrain. The processing has a number of distinctly different steps. First to appropriately prepare the imagery for processing we must destripe it and perform haze removal. Destriping can be done by the Horn and Woodham [1979] technique. Haze removal can be done by the Switzer, Kowalik and Lyon [1981] technique. These two steps constitute the preprocessing and are not discussed in this paper.

To a first order effect, after preprocessing the cause of the intensity value at any pixel is due to the combined effect of the angle at which the sun illuminates the ground patch corresponding to the pixel and the reflectance of the

surface material on the ground patch. To make sense of the spatial pattern first requires separating these two effects. For this purpose we modify the Eliason, Soderblom and Chavez [1981] technique to create two main images from the LANDSAT imagery. The first image is a reflectance image and the second image is a topographic modulation image which has information related to surface slope and sun illumination. The details of this technique are given in Section 2.

As discussed in Section 3, the reflectance image can be used by the Alfoldi and Munday [1978] procedure for identification of all areas of water. The topographic modulation image can be used to identify the ridges and the valleys. This is discussed in Section 4. With the valleys identified, each valley pixel may be assigned a relative elevation which increases as the valley path from the pixel to the river it empties in increases. Ridges must be assigned elevations higher than their neighboring valleys and each ridge pixel can be assigned a relative elevation which decreases on the ridge path from the pixel to the saddle point where the ridge crosses a valley. The ridge valley elevation assignment procedure is discussed in Section 5. Once ridges and valleys have been located and assigned relative elevations, a complete elevation model can be generated by interpolating values for non-ridge and non-valley pixels. The interpolation procedures are discussed in Section 6.

Since the launch of the first Earth Resources and Technology Satellite (ERTS, later renamed LANDSAT) in July 1972, much work in remote sensing has been done by using pattern analysis and picture processing techniques for image classification, restoration and enhancement. Few people have tried the scene analysis or artificial intelligence approach to describe the image in terms of the properties of objects or regions in the image and the relationships between them. Ehrich [1977] found global lineaments by partitioning the image into windows and applying long, straight linear filters at different orientations in each window to extract local evidence. Dynamic programming [Montanari, 1971; Martelli, 1972] was then used to form complete global lineaments. VanderBrug [1976] tested various detectors to get linear features in satellite imagery. This was only at the local level. Later VanderBrug [1977a] used relaxation to reduce noise in the output. Finally VanderBrug [1977b] defined a merit function that can be used to select pairs of segments to be merged so that local line detector responses can be linked together into a global representation of the curves. His work is closely related to the Shirai [1973] technique which employed sequential line following to find edges in scenes containing polyhedra. Li and Fu [1976] used tree grammars to locate highways and rivers from LANDSAT pictures. The above investigations deal with the extraction of all the linear features from an image, but they do not deal

with the interpretation of these linear features. In the following investigations, knowledge about the desired features are considered crucial in such analyses.

Bajcsy and Tavakoli [1975] argued that an image filter is not meaningful unless one has a world model, a description of the world one is dealing with. They recognized objects matching this description and filtered them out. This strategy is used to sequence the recognition of bridges, rivers, lakes, and islands from satellite pictures. Nagao and Matsuyama [1980] built an image understanding system that automatically located a variety of objects in an aerial photograph by using diverse knowledge of the world. It is one of the first image understanding systems that has incorporated very sophiscated artificial intelligence techniques into the analysis of complex aerial photographs. Fischler, Tenenbaum and Wolf [1981] designed a low-resolution road tracking (LRRT) algorithm for aerial imagery. The approach was based on a new paradigm for combining local information from multiple sources, map knowledge, and generic knowledge about roads. The final interpretation of the scene was achieved by using either graph search or dynamic programming.

Similarly, knowledge is important in our problem which requires analysis both at the local and global levels. Local level analysis will be discussed in Section 2 to 4; global level analysis will be discussed in Section 5 to 6.

## 2. Illumination model

The brightness and darkness in each band of LANDSAT images come from two main sources. First, they can be due to material properties. For example, in the spectral region (.8 - 1.1 μm) of band 7, water bodies absorb infrared radiation, so they appear as clearly delineated dark bodies; living vegetation reflects strongly in this portion of the infrared, so areas of living green vegetation appear as bright regions. Second, they may be due to topography and sun illumination angle effects. The mountain side facing to the sun appears as a bright region; the mountain side facing away from the sun may appear as a shadow or dark region. Unfortunately, the LANDSAT data values are some combination of these two effects. Eliason, Soderblom, and Chavez [1981] address this problem by defining an illumination model involving material reflectance and topographic modulation images. In the following, we will introduce a modified Lambertian model in which the information of diffuse light and shadows is also included.

For a pixel (x,y) which receives sunlight, the original LANDSAT image G measuring the amount of reflected light at band b is

$$G(x,y,b) = r(x,y,b)I(b)\cos\theta(x,y) + r(x,y,b)D(b) + H(b)$$

where r is the surface reflectance, I is illumination flux, $\theta$ is the angle between sun incidence direction and surface normal, D is diffuse light, and H is the haze due to atmospheric scattering. On the other hand, for a pixel (x,y) in shadow, G is simply

$$G(x,y,b) = r(x,y,b)\, D(b) + H(b)$$

After the haze H(b) is removed by the Switzer, Kowalick and Lyon [1981] technique, for pixels receiving sunlight, the ratio image of bands $b_1$ and $b_2$ is

$$\frac{G'(x,y,b_1)}{G'(x,y,b_2)} = \frac{G(x,y,b_1) - H(b_1)}{G(x,y,b_2) - H(b_2)}$$

$$= \frac{r(x,y,b_1)\,[I(b_1)\cos\theta(x,y) + D(b_1)]}{r(x,y,b_2)\,[I(b_2)\cos\theta(x,y) + D(b_2)]}$$

$$= \alpha \frac{r(x,y,b_1)}{r(x,y,b_2)}$$

if we assume $I(b_1) = \alpha I(b_2)$ and $D(b_1) = \alpha D(b_2)$.

Similarly, for pixels in shadows,

$$\frac{G'(x,y,b_1)}{G'(x,y,b_2} = \alpha \frac{r(x,y,b_1)}{r(x,y,b_2)}$$

In either case, the ratio is independent of $\cos\theta$. Thus, by clustering using different ratio images as features, the pixels grouped in one cluster should belong to the same ma-

terial reflectance group. The result is called a reflectance cluster image.

A window of 4-bands LANDSAT scene is shown in Figure 1. The image was taken in April 1976 over areas in Nicholas County, West Virginia and neighboring counties. The ratio images of 5/4, 6/5, 7/6 are shown in Figure 2, and the reflectance cluster image is shown in Figure 3.

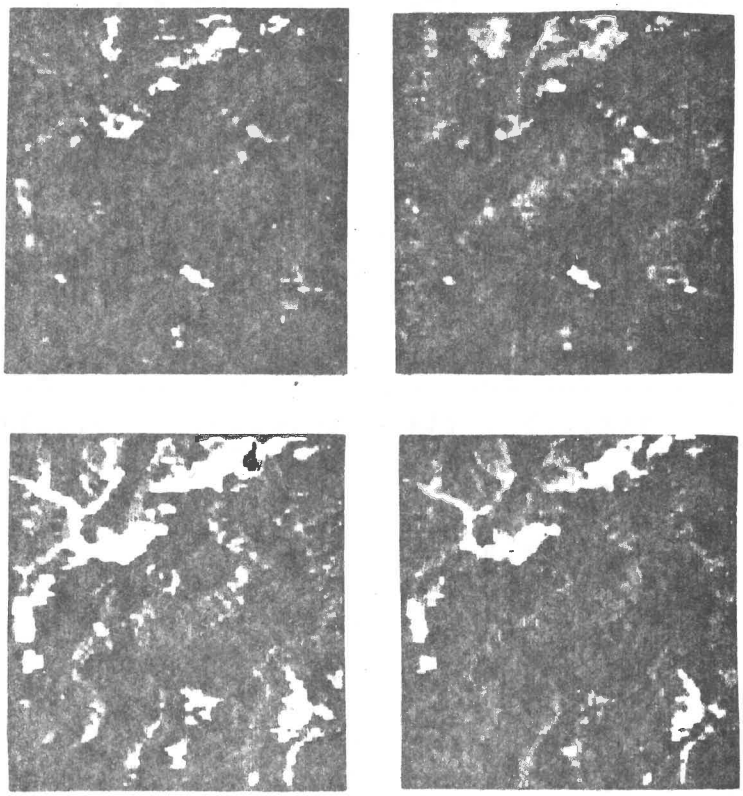

Figure 1 - 4- bands LANDSAT scene in W. Va.

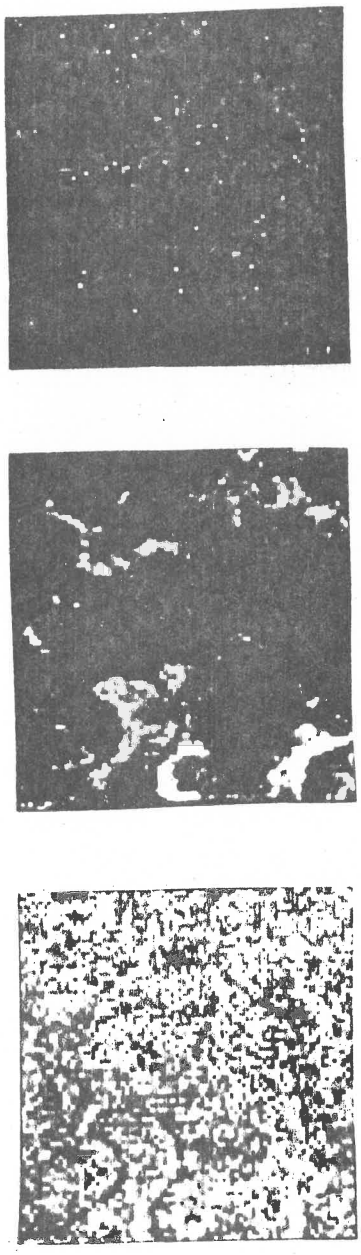

Figure 2 – Ratio images of 5/4, 6/5 and 7/6

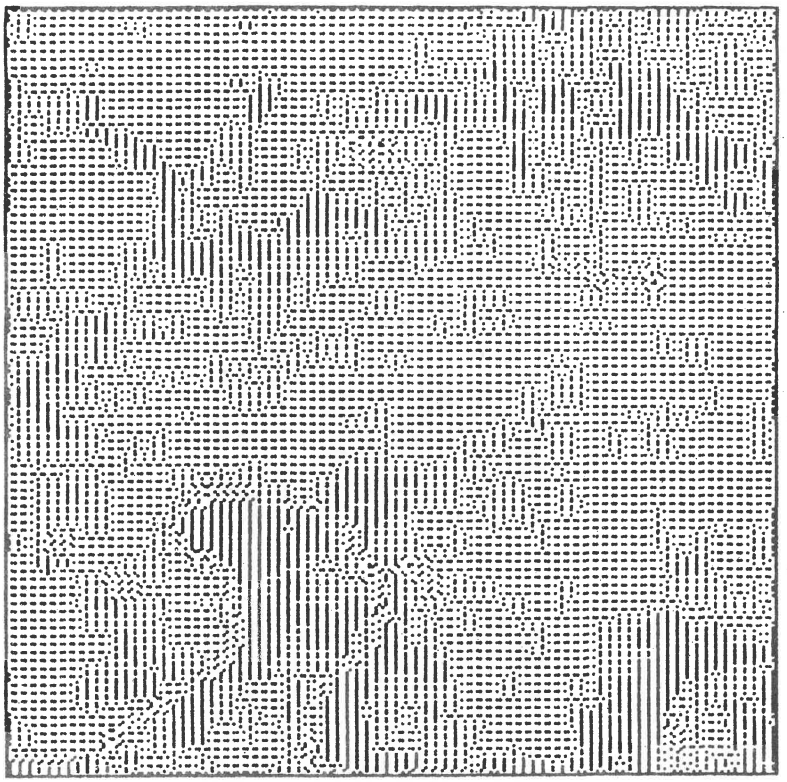

Figure 3 - Reflectance cluster image.

The reflectance cluster image is a function

$$R_c: \quad X \times Y \rightarrow \{1,2, ---, N_c\}$$

where X is the set of row coordinates, Y is the set of column coordinates, and $N_c$ is the total number of clusters. Each reflectance cluster cl is a subset of pixels defined by

$$C(cl) = \{(x,y) \mid R_c(x,y) = cl\},\ 1 \leq cl \leq N_c$$

The pixels in each C(cl) do not have identical gray tone intensities in the dehazed G′ image. This is due to the fact that some pixels are directly lit and others are in shadow. By performing a second clustering on G′ within each C(cl), we can split each C(cl) into a bright sub-cluster $C_0(cl)$ consisting of directly lit pixels and a dark sub-cluster $C_1(cl)$ consisting of pixels in shadow. A binary shadow image Sw can be defined by

$$Sw: X \times Y \rightarrow \{0,1\},$$

$$Sw(x,y) = \begin{cases} 0 \text{ if } (x,y) \in C_0(R_c(x,y)) \\ 1 \text{ if } (x,y) \in C_1(R_c(x,y)). \end{cases}$$

This is shown in Figure 4.

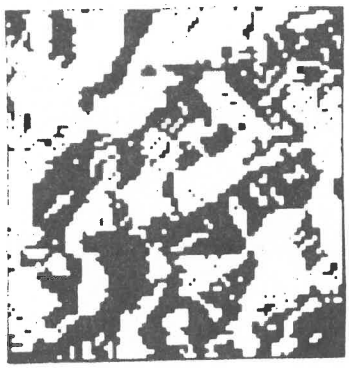

Figure 4 - Binary shadow image.

After the lit and shadowed pixels are identified, we extract a diffuse light image $D_f$ which contains in each pixel (x,y) the value r(x,y,b)D(b), a reflectance image R which contains in each pixel (x,y) the value r(x,y,b)I(b), and a topographic modulation image $T_p$ which contains in each pixel (x,y) the value cosθ(x,y). Thus, for directly lit pixels

$$G'(x,y,b) = R(x,y,b)\ T_p(x,y) + D_f(x,y,b), \qquad (*)$$

and for shadowed pixels

$$G'(x,y,b) = D_f(x,y,b)$$

Since shadowed pixels contain the information of diffuse light only, the mean dehazed G' value of pixels in $C_1(c1)$ can be used to represent the reflected diffuse light information for cluster c1. The diffuse lit image $D_f$ is defined by

$$D_f(x,y,b) = \sum_{(u,v)\ \varepsilon\ C_1(c1)} \frac{G'(u,v)}{\#\ C_1(c1)}$$

where $c1 = R_c(x,y)$. If the reflectance cluster image were perfect, we would have

Assumption 1 : r(x,y,b) is a constant $\bar{r}(c1,b)$ for all (x,y) in C(c1) with $c1 = R_c(x,y)$.

In this case,

$$D_f(x,y,b) = \bar{r}(c1,b)D(b) \sum_{C_1(c1)} \frac{1}{\#\ C_1(c1)}$$

$$= \bar{r}(c1,b)\ D(b)$$

Since directly lit pixels contain the information of diffuse light as well as direct sun illumination, the mean $G' - D_f$ value of pixels in $C_0(c1)$ can be used to represent the reflected sun illumination information for cluster c1. If pixel (x,y) is in reflectance cluster c1, that is, if $R_c(x,y) = c1$, then the reflectance image R can be defined by

$$R(x,y,b) = \sum_{(u,v)\ \varepsilon\ C_0(c1)} \frac{G'(u,v,b) - D_f(u,v,b)}{\#\ C_0(c1)}$$

$$= \bar{r}(c1,b)\ I(b) \sum_{C_0(c1)} \frac{\cos\theta(u,v)}{\#\ C_0(c1)}$$

$$= \bar{r}(c1,b)\ I(b)\ X_c(c1)$$

where $X_c$ is the spatial average of $\cos\theta$ for pixels in $C_0(c1)$. It is meaningful to look at R image only if we make the following assumption.

Assumption 2: $X_c(c1)$ takes the same value $X_c$ for all reflectance clusters.

Finally, from equation (*),

$$T_p(x,y) = \frac{G'(x,y,b) - D_f(x,y,b)}{R(x,y,b)}$$

$$= \frac{\cos\theta(x,y)}{X_c}$$

which contains the information about the cosine of the angle between the surface normal and the illumination direction. The $D_f$, R, and $T_p$ images for Figure 1 are shown in Figure 5,6, and 7.

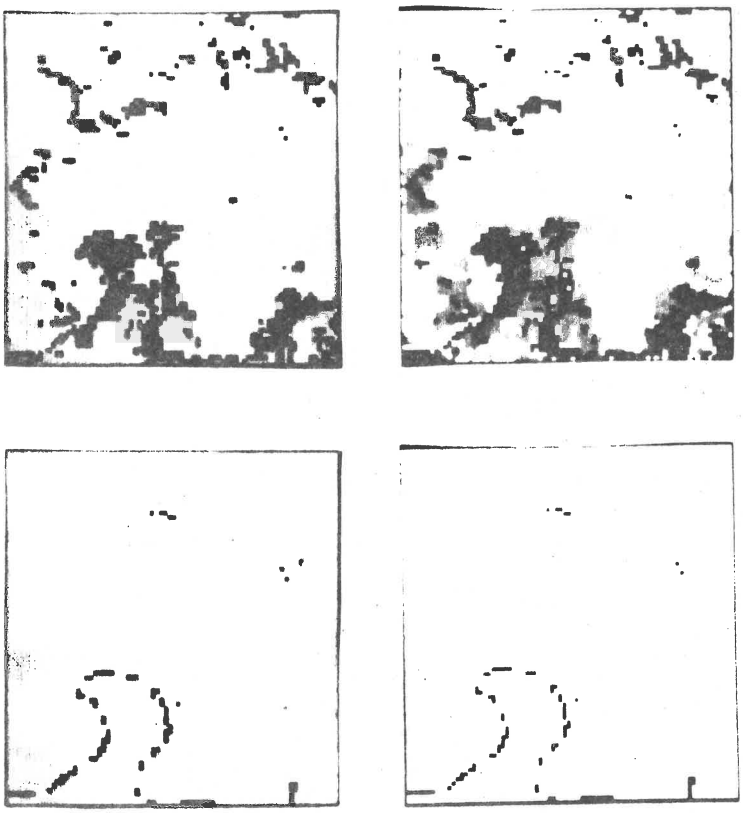

Figure 5 - Diffuse light image.

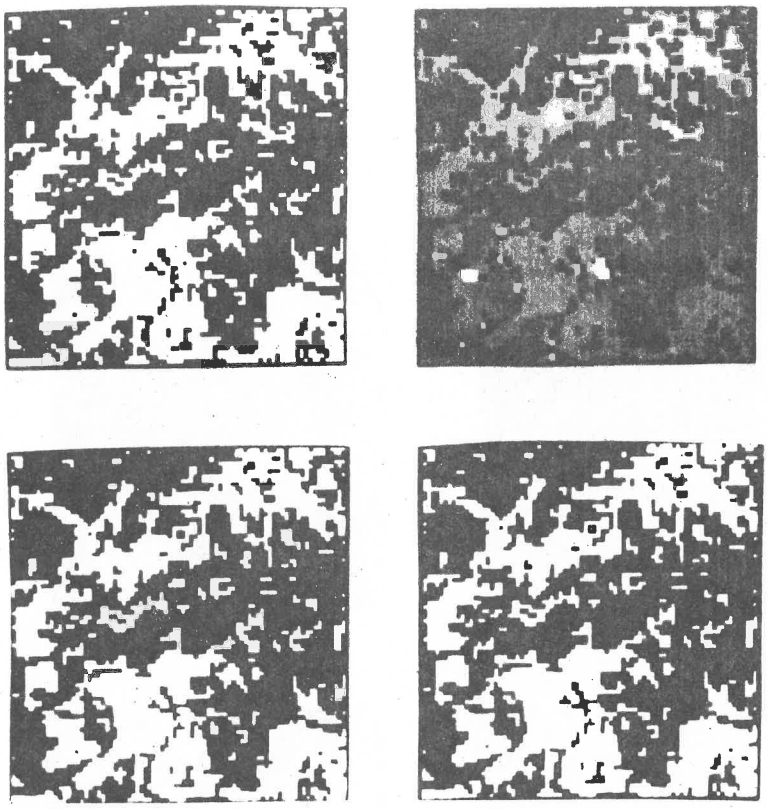

Figure 6 - Reflectance image.

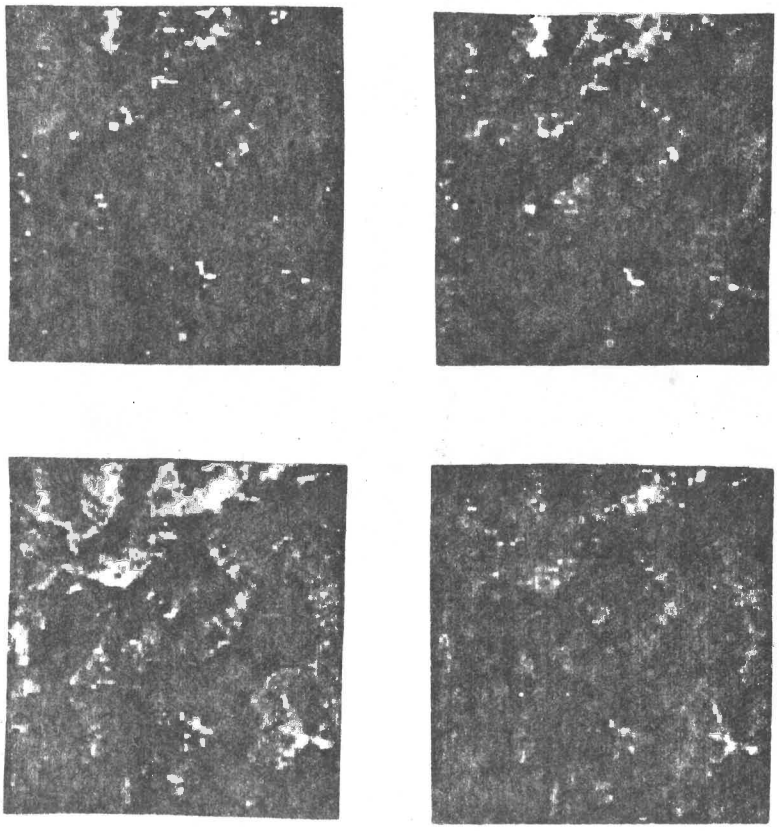

Figure 7 - Topographic modulation image.

## 3. Detection of Visible Rivers

Visible river detection can play an important part in generating an elevation model since elevations away from the river must increase. Visible rivers can be detected using the material reflectance image created by the technique discussed in the last section. In the spectral region (.8 - 1.1 μm) of band 7, water bodies absorb infrared radiation, so visible rivers appear as dark curves, and lakes appear as dark regions. In the material reflectance image of band 7, these dark features become more clear because shadows are removed. However, not all dark features are water bodies; the real water bodies can be identified by the following process [Alfoldi and Munday, 1978].

(1) A band 4 green coefficient x of every pixel is calculated as the ratio of the radiance of band 4 over the radiance sum of bands 4, 5 and 6. Similarly a band 5 red coefficient y is calculated for every pixel. X and y are called LANDSAT chromaticity coordinates.

(2) In this coordinate system, Munday [1974] has determined a curve (Figure 8) which is the locus of the positions of chromaticity values of water bodies. If, for some pixels, the x, y values calculated in 1 are close to this curve, then those pixels can be identified as portions of water bodies.

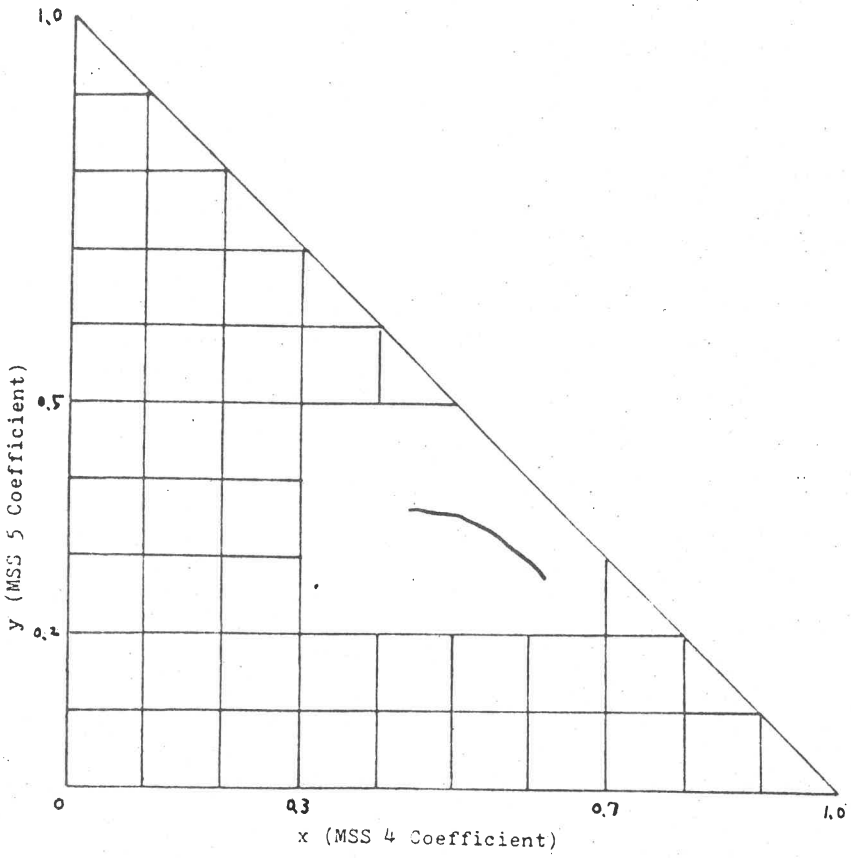


**Figure 8 - Chromaticity plot.**

## 4. Ridge-Valley Detection

In this section, we describe how to extract shadowed and bright areas, create linear features on the borders between these areas, and then classify these linear features into ridge and valley segments. In the next two sections, we discuss how to generate a relative elevation model.

From the shadow image of Figure 4, we can get the connected components of bright and shadowed regions. Because valleys and ridges exist on the borders between these regions, the perimeters of these bright and shadowed regions are segmented into border segments according to their left regions, right regions, and orientations. A border segment is a maximally long sequence of connected pixels which are on the border between two given regions. Because the detection of ridges and valleys is highly orientation-dependent and the sun illumination comes from east in Figure 1, each border segment is further broken into several pieces according to orientation: all the east-west parts can be separated from the north-south parts. The result is shown in Figure 9.

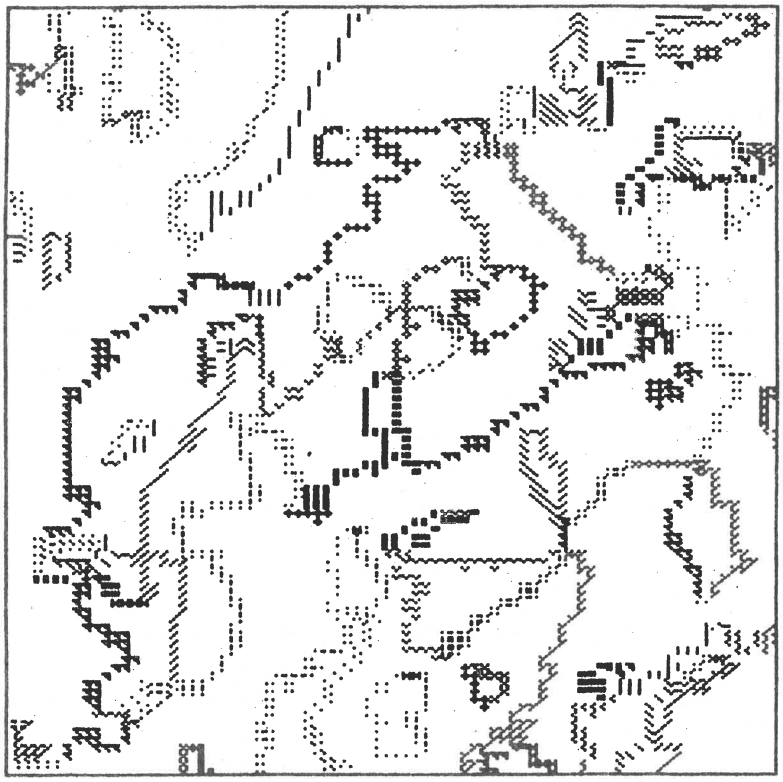

Figure 9 - Border Segments

As the sun illumination comes from east, those border segments which are valley segments or ridge segments can be identified according to the brightness of their left and right regions. Because most of the trees in this area in April are unfoliated, the strongest region boundaries are shadow boundaries rather than tonal boundaries, and the strongest boundaries are those at the extremes of steep slopes oriented normal to the sun direction. Because the sun illumination is predominantly east-west, a boundary that is dark on the left and bright on the right will correspond to a ridge, and the reverse will correspond to a valley.

East-west region boundaries are classified according to the labeling of neighboring north-south boundaries as well as their orientation relative to the east-west boundaries. As shown in Figure 10, east-west boundaries have the same labeling of the north-south boundary which makes the angle between them larger. The results of ridge-valley finding are shown in Figure 11. Assignment of relative elevation to ridge and valley is discussed in the next section.

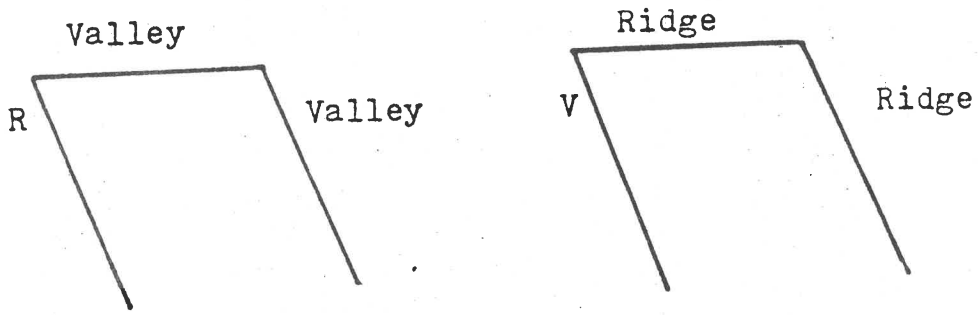


Figure 10 - Classifying east-west border segments.

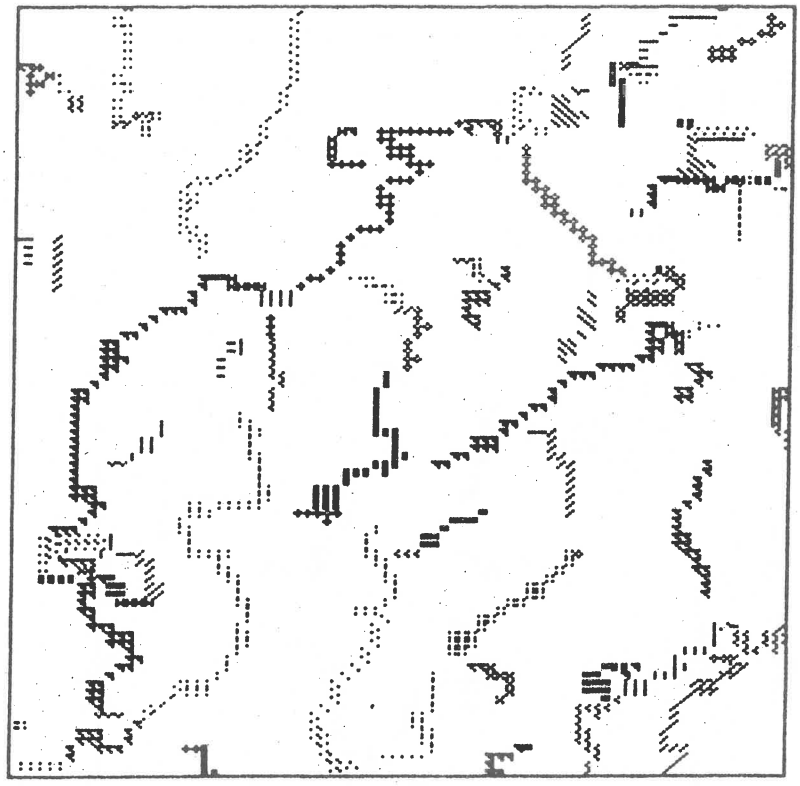

Figure 11 - a. Valley map consisting of the border segments which are identified as valleys.

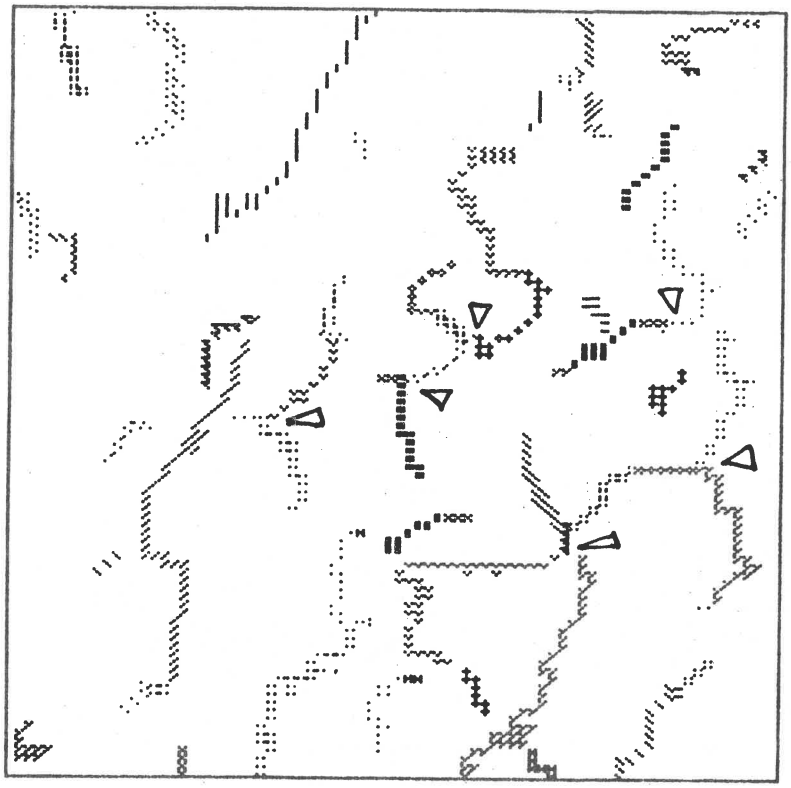

Figure 11 - b. Ridge map consisting of the border segments which are identified as ridges.

## 5. Relative Elevations of Ridge and Valley Segments

In this section, we describe how to estimate the relative elevations of the ridges and valleys. First we will describe a model which can do the elevation assignment job, then we will give the equations of elevation assignment.

Assuming that we have a stream network in a mountainous area, and we know where the biggest rivers are, we can trace the network, starting from the biggest rivers, to find the flow directions of all the stream segments because water always flows from higher locations to lower locations. In other words, if the valley segments detected in the last section formed a network, then starting from the visible rivers detected in Section 3, we can trace the network and assign relative elevations to all the segments. Unfortunately, the observed valley segments do not form a network; there are many gaps. As shown in Figure 12, if it is dark on the right and bright on the left of stream Vb, then Vg cannot be detected due to the shadow on the right of Vb, and a gap exists between Vb and a smaller stream Vs.

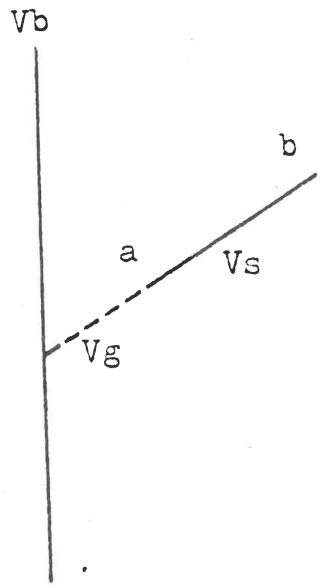


Figure 12 - The gap between a smaller and a larger stream.

The knowledge that the cross-sections of valleys are V-shaped can be used to bridge the gaps. If one looks at topographic maps, the elevation contours of valleys such as in Figure 13 can be frequently found. Thus, if one draws a line ab perpendicular to the valley Va, the elevations are

increasing from point o to point a , and also from point o to point b. However, if a ridge point is encountered during the process, the increasing has to stop because the elevation starts to decrease. Thus the route of growth is directed both by the valleys and by the ridges, in other words, by global information.

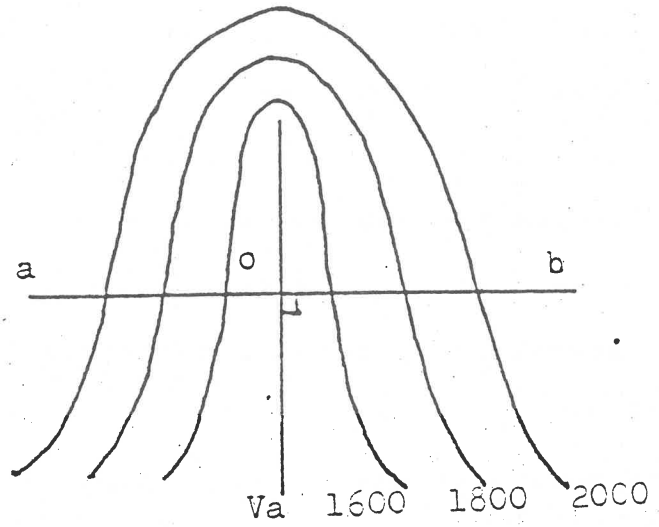


Figure 13 - The elevation pattern of valleys and its relation to elevation growing

Applying this idea to Figure 12 and assuming that growing propagates away from valley segment Vb, the end a of valley segment Vs will be touched first by this growing, and it is

deduced that end b of Vs must be higher than end a. This is the basic idea for determining the higher-lower ends of all the valley segments. The elevations of all the points in one segment can be calculated if we know its slope. On the other hand, ridges get elevations when the growing stops at them. Now, we will give the simple equations of elevation assignment.

Our elevation growing model simply assumes that elevation increases monotonically from valleys to ridges or along valley segments from rivers to the saddles where a valley crosses a ridge. It can be used for assigning initial relative elevations to each pixel. Because no attempt is made to realistically account for the topographic shape of the hillsides from the valley to the ridge, the initial relative elevations will be more accurate for the ridge or valley labeled pixels than the non-ridge and non-valley labeled pixels. Section 6 discusses a more realistic procedure for hillside elevation estimation using the ridge valley elevations calculated in this section.

There are two ways a pixel can get assigned an elevation depending on whether the pixel belongs to a valley segment or whether the pixel does not belong to a valley segment. Let U be the set of valley segments. Two slopes are associated with each valley segment Vs in U: Sv(Vs) and Sp(Vs).

Sv(Vs) is the slope along Vs itself. Sp(Vs) is the slope of lines outside of Vs and perpendicular to Vs.

The elevation growing model constructs the elevation function El: Zr X Zc -> Ip, where Zr is the set of row coordinates, Zc is the set of column coordinates, and Ip is the set of zero and positive integers. If p is a pixel belonging to a valley segment Vs and p1 is the lower end pixel identified as in Figure 12, then

$$El(p) = El(p1) + Sv(Vs) * Dist(p, p1)$$

where Dist is the Euclidean distance between two pixels.

If p does not belong to any valley segment, and its elevation is originated from pixel pr of valley segment Vs, then

$$El(p) = El(pr) + Sp(Vs) * Dist(p, pr).$$

In a small area, one can assume the elevations of visible rivers are lowest. Assigning some initial elevation values to the pixels of the valley segments classified as visible rivers, the elevations of all the other pixels in the image window can be related to the initial elevations of visible river segments by repeatedly using the above two equations. The relative heights of valley segments created by elevation growing model are indicated by arrows in Figure 14, and the ground truth is shown in Figure 15.

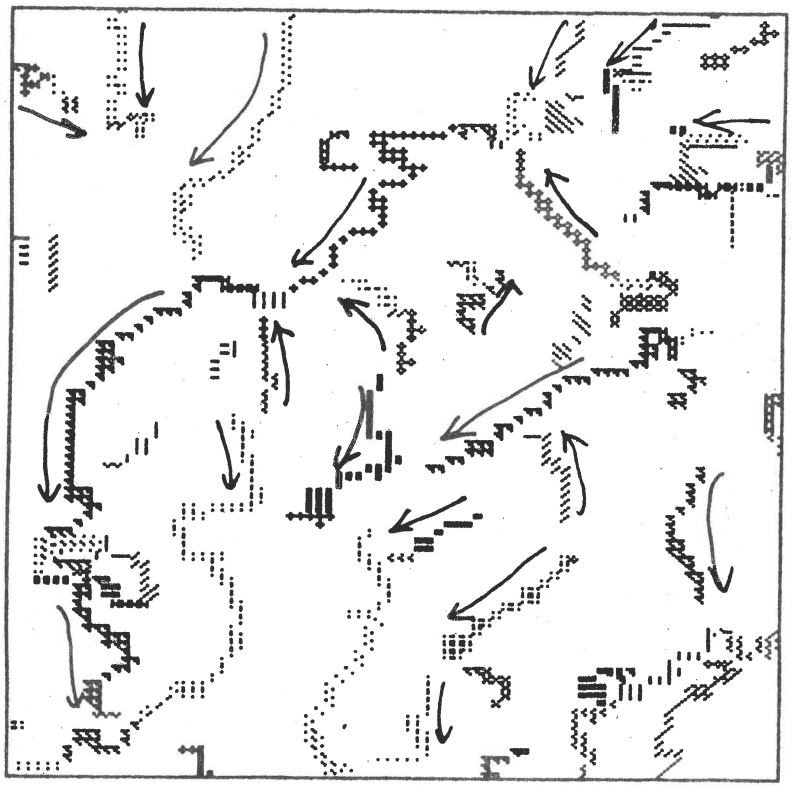

Figure 14 - Relative elevations of valley segments. The arrow are from high ends to low ends.

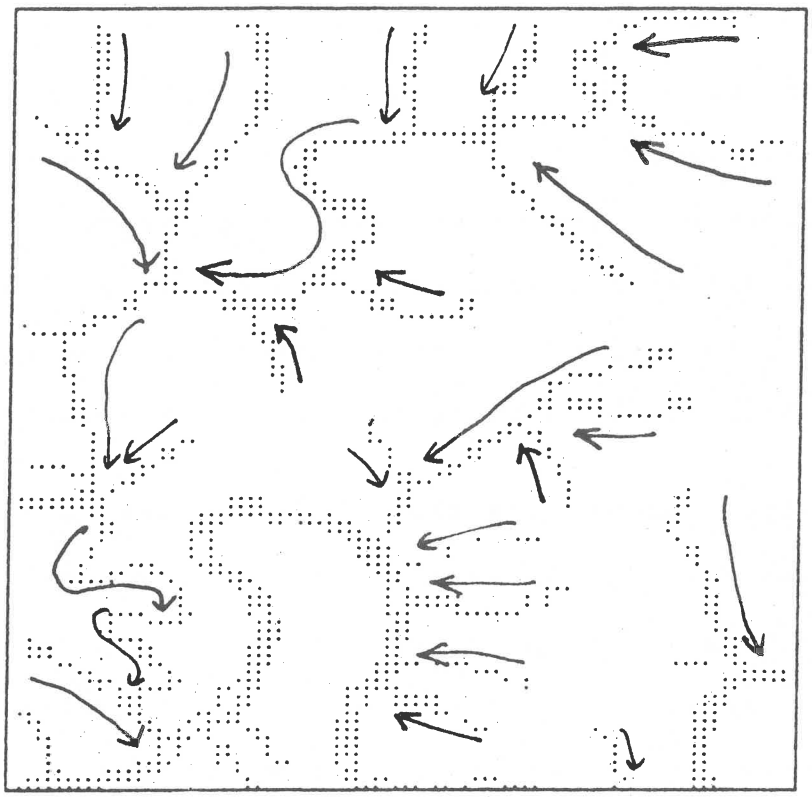

Figure 15 - Stream map created from ground truth.

## 5.1 Identification of Peak Junctions

When several valleys and ridges point toward a junction, very often this juction is a peak (peak at junction). The peak itself is formed by the junction of several ridges that radiate outward from the peak. (The idealized situation represented in Figure 16 shows four symetrically oriented ridges; in our area, real peaks are often formed by junctions of two or three ridges.) Ridges of course are separated by valleys, so the higher tips of valley segments tend to point toward peaks. The ridge segments intersect to form a peak, whereas valley segments tend to point towards peaks, without actually joining. In this subsection, we discuss the criteria which can be used to identify peak junctions.

Because ridge segments are the major features of peaks, we make the constraint that the number of ridge segments at a junction is larger than the number of valley segments. For many situations, it seems reasonable to relate the heights of peaks to the lengths of ridges that form the peaks. For our class of topographic forms (for example), it is unlikely that very high peaks can be formed by the intersection of very short ridges. As a result, to exclude very low peaks and false peaks from consideration, we impose a rather arbitrary constraint upon definitions of peaks. Currently, we define a peak junction as a junction composed of

four border segments, with the number of its ridge segments larger than the number of valley segments, and the length of its longest ridge segment longer than 800 meters. The peaks thus located in Figure 1 are marked as triangles in Figure 11.b. The correspondence between this result and the topographical map is suprisingly good.

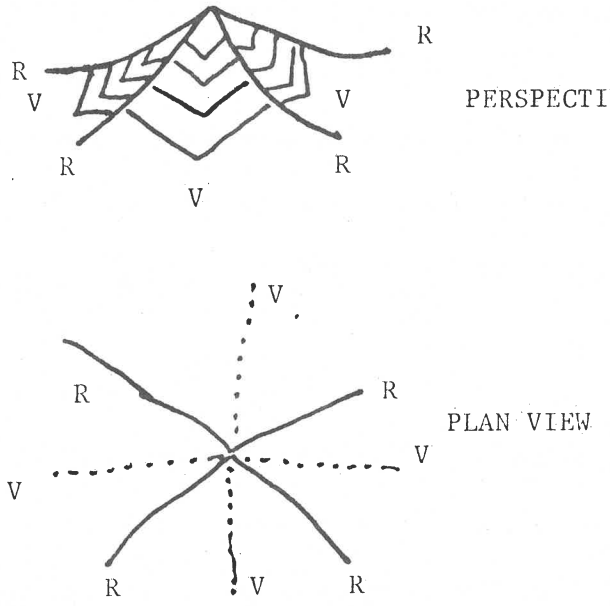


Figure 16 - Idealized relationships between peaks, valleys, ridges.

## 6. Interpolating Between Ridges and Valleys

In the last section all pixels were assigned elevations, but because realistic shape of the hillsides from valleys to ridges were not taken into account, only the relative elevations of the ridges and valleys are held to be accurate. In this section we describe a few interpolation procedures which permit more realistic elevation assignment to non-valley and non-ridge pixels.

The first interpolating surface has the given elevation values at ridges and valleys and has a 3 X 3 digital Laplacian of zero at all non-ridge and non-valley pixels. This will be referred to as the Laplacian surface. The system of linear equations which this constraint gives rise to can be written as

$$A\,x = b.$$

The vector x is the solution and represents the values to be assigned to each 'variable' (non-ridge non-valley) pixel in the elevation model. The A matrix is defined by applying the digital Laplacian mask operator (Figure 17) to each variable pixel. A mask operator is applied to a pixel by placing the mask over the image so that the central (large positive) mask value is directly over the pixel whose value is to be computed. The pixel value is changed to make the sum of the mask values times the corresponding image values under them equal to zero. For the Laplacian surface only,

Neumann boundary conditions are enforced along the outside rows and columns of the elevation model image. That is, the outer-most row or column is repeated so that the mask operator can be applied to the outside pixels. There is one row in A for each variable pixel in the elevation model and one coefficient value in that row for each variable. A is a sparse matrix since no variable is constrained by more than four other variables (due to the definition of the digital Laplacian mask operator). The b vector is the right hand side of each of the linear equations in the system. The constants on the left hand side of each equation (that result from applying the Laplacian operator to a variable pixel that has a known pixel 4-adjacent to it) are carried to the right hand side and appear in b. For equations representing variable pixels not 4-adjacent to known pixels, the corresponding b element is zero.

$$\begin{array}{ccc} & -1 & \\ -1 & 4 & -1 \\ & -1 & \end{array}$$

Figure 17 - A digital Laplacian mask

The second interpolating surface has the given boundary values and minimizes the quadratic variation of the result-

ing surface [Grimson, 1981]. The boundary conditions with which the surface must agree are depth values along the zero-crossings. If the surface elevation function is E and subscripts denote partial differentiation, then the final surface E minimizes

$$\iint (E^2_{xx} + 2\,E^2_{xy} + E^2_{yy})\; d_x\, d_y$$

Since the surface function can be converted to a discrete grid format, the differential operators can be converted to difference operators, and the double integral can be converted to double summation, the solution of the above function can be formed by setting up a discrete corresponding set of linear equations

$$Q\ x = b.$$

The x and b vectors have the same meaning as in the Laplacian case and are constructed similarly. The Q matrix is likewise similar to the A matrix of the Laplacian. Instead of using Neumann boundary conditions at the edge of the image, the quadratic variation surface is defined by using special masks to fit the rows and columns near the outside edges. The six masks (Figure 18) are rotated as necessary and applied to the only appropriate variable pixels of the elevation image to define Q. Mask two is applied to corner pixels, mask three is applied to pixels in the outside row or column that are adjacent to a corner pixel, mask four is applied to other pixels in the outside rows and columns,

mask five is applied to pixels in the next-to-the outside row and columns that are 8-adjacent to corner pixels, mask six is applied to other pixels in the next to the outside rows and columns, and mask 1 is applied to all other variable pixels in the image.

$$\begin{array}{ccccc} & & 2 & & \\ & 4 & -16 & 4 & \\ 2 & -16 & 40 & -16 & 2 \\ & 4 & -16 & 4 & \\ & & 2 & & \end{array}$$

(1)

$$\begin{array}{ccc} & 2 & \\ -8 & & \\ 8 & -8 & 2 \end{array}$$

(2)

$$\begin{array}{ccccc} & & 2 & & \\ & 4 & -12 & 4 & \\ -8 & & 20 & -12 & 2 \end{array}$$

(3)

$$\begin{array}{ccccc} & & 2 & & \\ & 4 & -12 & 4 & \\ 2 & -12 & 22 & -12 & 2 \end{array}$$

(4)

$$\begin{array}{ccccc} & & 2 & & \\ & 4 & -16 & 4 & \\ -12 & & 36 & -16 & 2 \\ & 4 & -12 & 4 & \end{array}$$

(5)

$$\begin{array}{ccccc} & & 2 & & \\ & 4 & -16 & 4 & \\ 2 & -16 & 38 & -16 & 2 \\ & 4 & -12 & 4 & \end{array}$$

(6)

Figure 18 - Six masks for the quadratic variation method.

The third kind of interpolation surfaces can be created without using any mask. For each non-boundary pixel, we can first find its distances to the nearest valley pixels and nearest ridge pixels. From these distances and the elevations at these nearest valley pixel and nearest ridge pixel, either a linear, cubic, or fifth order fit interpolation can be used to calculate the elevation of this non-boundary pixel. If cubic fit is used, the first order derivative is zero at ridge and valley pixels. If fifth order fit is used, both the first and second order derivatives are zero at ridge and valley pixels. The resulting images with higher brightness indicating higher elevation and the corresponding surface plots are shown in Figure 19. The image and surface plot of the elevations read from digital terrain tape [NCIC, 1980] for this area are shown in Figure 20. The reconstructed LANDSAT images by using diffuse light image (Figure 5), reflectance image (Figure 6), elevation model (Figure 19a), and an artificial sun at specified azimuth and elevation angles are shown in Figure 21. They are reasonable reconstructions.

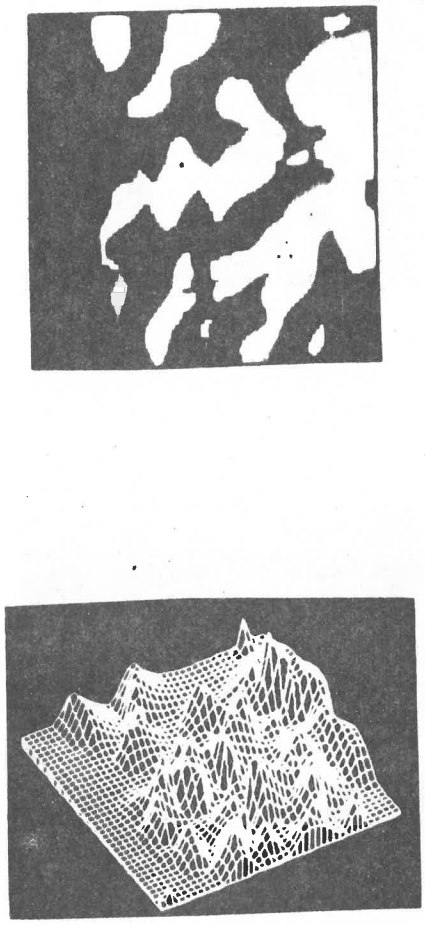

Figure 19a. Elevation Model by Method 1, Laplacian Mask

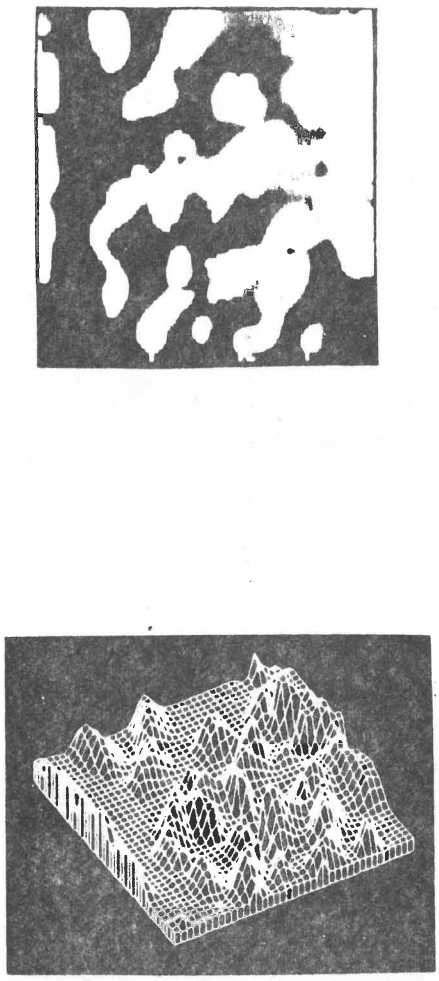

Figure 19b. Elevation Model by Method 2, Quadratic variation

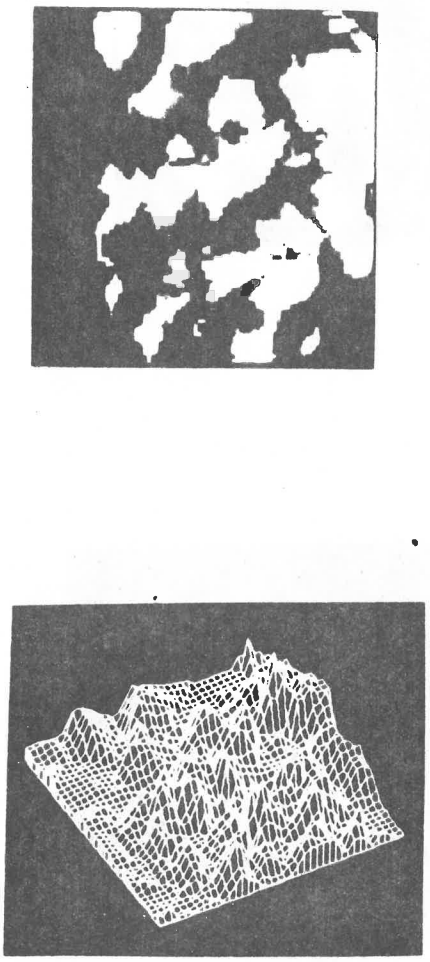

Figure 19c. Elevation Model by Method 3, Linear fit

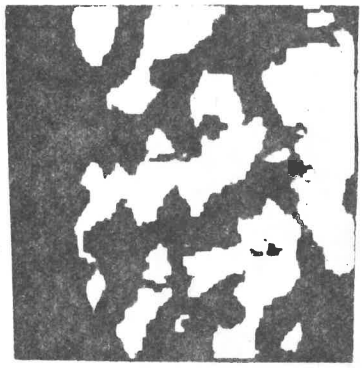

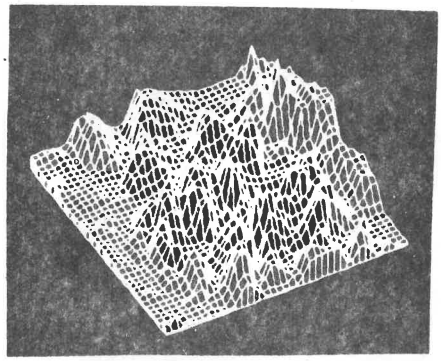

Figure 19d. Elevation Model by Method 3, Cubic fit

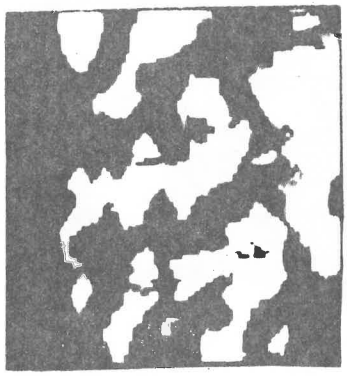

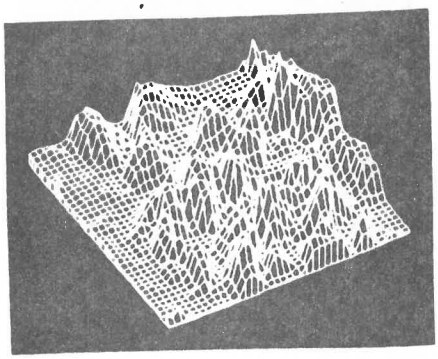

Figure 19e. Elevation Model by Method 3, Fifth order fit

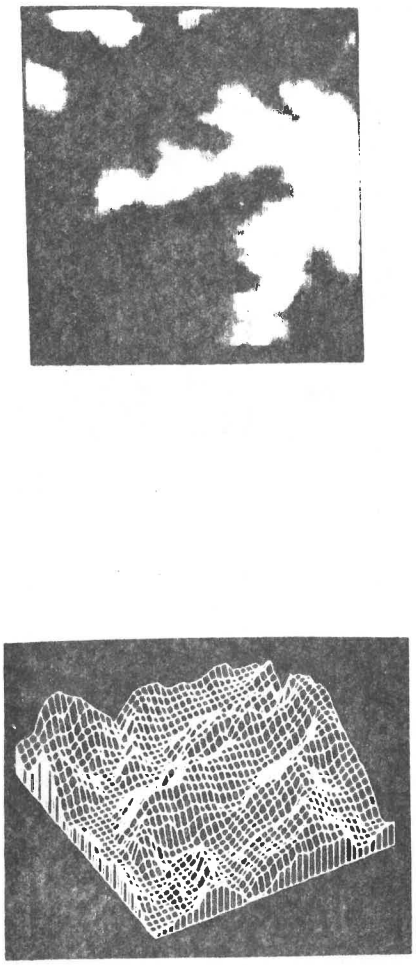

Figure 20 - Elevation model from digital terrain tape.

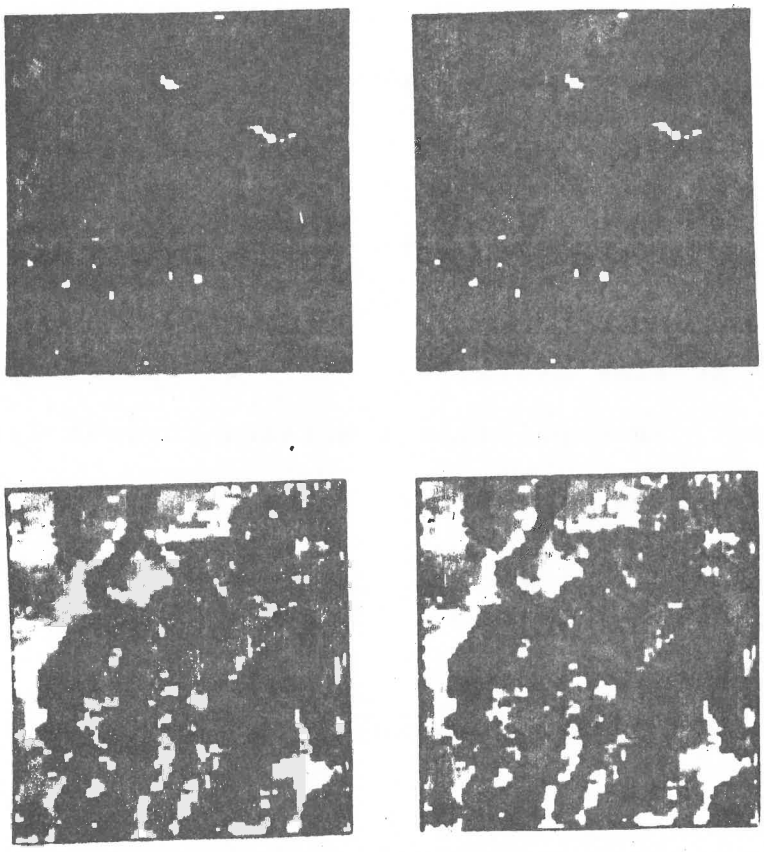

Figure 21 - Reconstructed LANDSAT imagery

## 7. Conclusion

In order to reconstruct 3D spatial information from LANDSAT imagery, we need to identify shadowed and directly lit pixels as well as local slope information. A model involving reflectance, topography, diffuse light, and haze has been discussed and a technique for computing this information has been given. The shadow reflectance, and elevation images look quite good by comparing with the topographic map of the same area and our understanding of the vegetation surface cover.

Once the shadow image and local slope information is determined, ridge and valley segments are detected and then an elevation growing model is used to assign relative elevations to them. Interpolation generates surface elevation at all locations from the known values at ridge and valley segements.

## Acknowledgement

The authors want to thank J. Campbell, R.W. Ehrich, and L.G. Shapiro for their helpful suggestions and discussions.

## References

T.T. Alfoldi and J.C. Munday, Jr., Water Quality Analysis by Digital Chromaticity Mapping of LANDSAT Data, Canadian J. of Remote Sensing, 4 (2): 108 - 126, 1978.

R. Bajcsy and M. Tavakoli, Image Filtering = a Context Dependent Process, IEEE Trans. on Circuits and Systems, May 1975.

R.W. Ehrich, Detection of Global Edges in Textured Images, IEEE Trans. on Computers, Vol. C-26, June 1977, pp. 589-603.

P.T. Eliason, L.A. Soderblom, and P.S. Chavez, Jr., Extraction of Topographic and Spectral Albedo Information from Multispectral Images, Photogrammetric Engineering and Remote Sensing, Vol. 48, No. 11, Nov. 1981, pp. 1571-1579.

M.A. Fischler, J.M. Tenenbaum and H.C. Wolf, Detection of Roads and Linear Structures in Low-Resolution Aerial Imagery Using a Multisource Knowledge Integration Technique, Computer Graphics and Image Processing, Vol. 15, 1981, pp. 201-223.

W.E.L. Grimson, An Implementation of a Computational Theory of Visual Surface Interpolation MIT AI Memo, 1981.

B.K.P. Horn and R.J. Woodham, Destriping LANDSAT MSS Images by Histogram Modification, Computer Graphics and Image Processing, Vol. 10, 1979, pp. 69-83.

R.Y. Li and K.S. Fu, Tree System Approach for LANDSAT Data Intepretation, Proceedings of the IEEE Symposium in Machine Processing of Remotely Sensed Data, June 1976.

A. Martelli, Edge Detection Using Heuristic Search Methods, Computer Graphics and Image Processing, Vol.1, pp.169-182, 1972.

U. Montanari, On the Optimal Detection of Curves in Noisy Pictures, CACM, Vol.18, pp.335-345, 1971.

J.C. Munday, Jr., Lake Ontario Water Mass Determination from ERTS-1, Proc. 9th Intl. Symp. Remote Sensing of Environment, ERIM, Ann Arbor, pp. 1355-1368, 1974.

M. Nagao and T. Matsuyama, A Structural Analysis of Complex Aerial Photographs, Plenum Press, 1980.

National Cartographic Information Center, Digital Terrain Tapes, User Guide, Second Edition, 1980.

Y. Shirai, A Context Sensitive Line Finder for Recognition of Polyhedra, Artificial Intelligence, Vol.4, pp.95-119, 1973.

P.Switzer, W.S. Kowalik and R.J.P. Lyon, Estimation of Atmospheric Path-Radiance by the Covariance Matrix Method, Photogrammetric Engineering and Remote Sensing, Oct., 1981, pp. 1469-1476.

G.J. Vanderbrug, Line Detection in Satellite Imagery, IEEE Trans. on Geoscience Electronics, Vol. GE-14, Jan. 1976, pp. 37-44.

[1977a] G.J. VanderBrug, Experiments in Iterative Enhancement of Linear Features, Computer Graphics and Image Processing, Vol. 6, 1977, pp. 25-42.

[1977b] G.J. Vanderbrug, Curve Representation and Mapping, Computer Science Technical Report TR-561, U. of Maryland, Aug. 1977.

R.L. Wildey, Generalized Photochinometry for Mariner 9, Icarus, Vol.75, pp.613-626, 1975.